



Architecture of the crust and uppermost mantle in the northern Canadian Cordillera from receiver functions

Alizia Tarayoun, Pascal Audet, Stephane Mazzotti, Azadeh Ashoori

► To cite this version:

Alizia Tarayoun, Pascal Audet, Stephane Mazzotti, Azadeh Ashoori. Architecture of the crust and uppermost mantle in the northern Canadian Cordillera from receiver functions. *Journal of Geophysical Research : Solid Earth*, 2017, 122 (7), pp.5268-5287. 10.1002/2017JB014284 . hal-01685550

HAL Id: hal-01685550

<https://hal.science/hal-01685550>

Submitted on 16 Jan 2018

HAL is a multi-disciplinary open access archive for the deposit and dissemination of scientific research documents, whether they are published or not. The documents may come from teaching and research institutions in France or abroad, or from public or private research centers.

L'archive ouverte pluridisciplinaire **HAL**, est destinée au dépôt et à la diffusion de documents scientifiques de niveau recherche, publiés ou non, émanant des établissements d'enseignement et de recherche français ou étrangers, des laboratoires publics ou privés.

Journal of Geophysical Research: Solid Earth**RESEARCH ARTICLE**

10.1002/2017JB014284

Key Points:

- We constrain crust and uppermost mantle structure in the northern Canadian Cordillera using receiver functions
- Moho is sharp and flat at 32 ± 2 km, and we find upper crustal and sub-Moho anisotropic layers likely related to Cordilleran evolution
- Lateral and vertical variations in seismic anisotropy allow revision of geodynamic models proposed to explain active tectonic deformation

Supporting Information:

- Supporting Information S1

Correspondence to:

P. Audet,
pascal.audet@uottawa.ca

Citation:

Tarayoun, A., P. Audet, S. Mazzotti, and A. Ashoori (2017), Architecture of the crust and uppermost mantle in the northern Canadian Cordillera from receiver functions, *J. Geophys. Res. Solid Earth*, 122, 5268–5287, doi:10.1002/2017JB014284.

Received 5 APR 2017

Accepted 20 JUN 2017

Accepted article online 21 JUN 2017

Published online 12 JUL 2017

Architecture of the crust and uppermost mantle in the northern Canadian Cordillera from receiver functions

Alizia Tarayoun¹ , Pascal Audet² , Stéphane Mazzotti¹ , and Azadeh Ashoori²

¹Geosciences Montpellier, Université de Montpellier, Montpellier, France, ²Department of Earth and Environmental Sciences, University of Ottawa, Ottawa, Ontario, Canada

Abstract The northern Canadian Cordillera (NCC) is an active orogenic belt in northwestern Canada characterized by deformed autochthonous and allochthonous structures that were emplaced in successive episodes of convergence since the Late Cretaceous. Seismicity and crustal deformation are concentrated along corridors located far (>200 to ~800 km) from the convergent plate margin. Proposed geodynamic models require information on crust and mantle structure and strain history, which are poorly constrained. We calculate receiver functions using 66 broadband seismic stations within and around the NCC and process them to estimate Moho depth and *P*-to-*S* velocity ratio (V_p/V_s) of the Cordilleran crust. We also perform a harmonic decomposition to determine the anisotropy of the subsurface layers. From these results, we construct simple seismic velocity models at selected stations and simulate receiver function data to constrain crust and uppermost mantle structure and anisotropy. Our results indicate a relatively flat and sharp Moho at 32 ± 2 km depth and crustal V_p/V_s of 1.75 ± 0.05 . Seismic anisotropy is pervasive in the upper crust and within a thin (~10–15 km thick) sub-Moho layer. The modeled plunging slow axis of hexagonal symmetry of the upper crustal anisotropic layer may reflect the presence of fractures or mica-rich mylonites. The subhorizontal fast axis of hexagonal anisotropy within the sub-Moho layer is generally consistent with the SE-NW orientation of large-scale tectonic structures. These results allow us to revise the geodynamic models proposed to explain active deformation within the NCC.

1. Introduction

The northern Canadian Cordillera is a high-elevation, low-relief orogenic belt in northwestern Canada (Figure 1a). It is one of the most seismically active regions in North America, where earthquakes are distributed within four main corridors: the Denali Fault-St. Elias system to the southwest, the Mackenzie Mountains ~800 km to the east, the Richardson Mountains to the north, and to a lesser extent the Tintina Fault area across central Yukon [Mazzotti *et al.*, 2008]. Lateral strike-slip earthquakes dominate the most active corridor along the transpressive Denali Fault system, with some thrust earthquakes accommodating the north directed convergence of the Yakutat Block in southeast Alaska. The other corridors are much farther away from plate boundary forces, yet they exhibit active seismicity with large historical earthquakes (e.g., the magnitude $M 6.9$ Nahanni earthquake in 1969) [Wetmiller *et al.*, 1988].

Tectonic models have been developed to describe such deformation. One of the leading models, referred to as the “orogenic float” model [Oldow *et al.*, 1990], proposes a thin and rigid upper crustal layer, decoupled from the underlying weak lower crust and mantle due to elevated geotherm, which is pushed horizontally at the plate boundary to the west and transmits stresses throughout the Cordillera [Mazzotti and Hyndman, 2002; Hyndman *et al.*, 2005]. The compressive stresses reactivate the Mesozoic fold-and-thrust belt at the Cordilleran Deformation Front, which generates seismic activity far from the plate boundary. The orogenic float model is supported by numerous geophysical observations that indicate a flat, shallow Moho (~35 km depth [e.g., Clowes *et al.*, 2005]), elevated upper mantle temperatures [e.g., Lewis *et al.*, 2003], and low effective elastic thickness (<10 km [e.g., Flück *et al.*, 2003; Audet *et al.*, 2007]) pointing to a mechanical decoupling between a strong upper crust and a weak lower crust and uppermost mantle. Under this framework, recent tectonics of the cordillera should result in decoupled structures, limited to the upper crust.

In contrast with the orogenic float, Finzel *et al.* [2011, 2014, 2015] propose an alternative tectonic model based on the net surface deformation produced by a combination of buoyancy forces due to gravitational

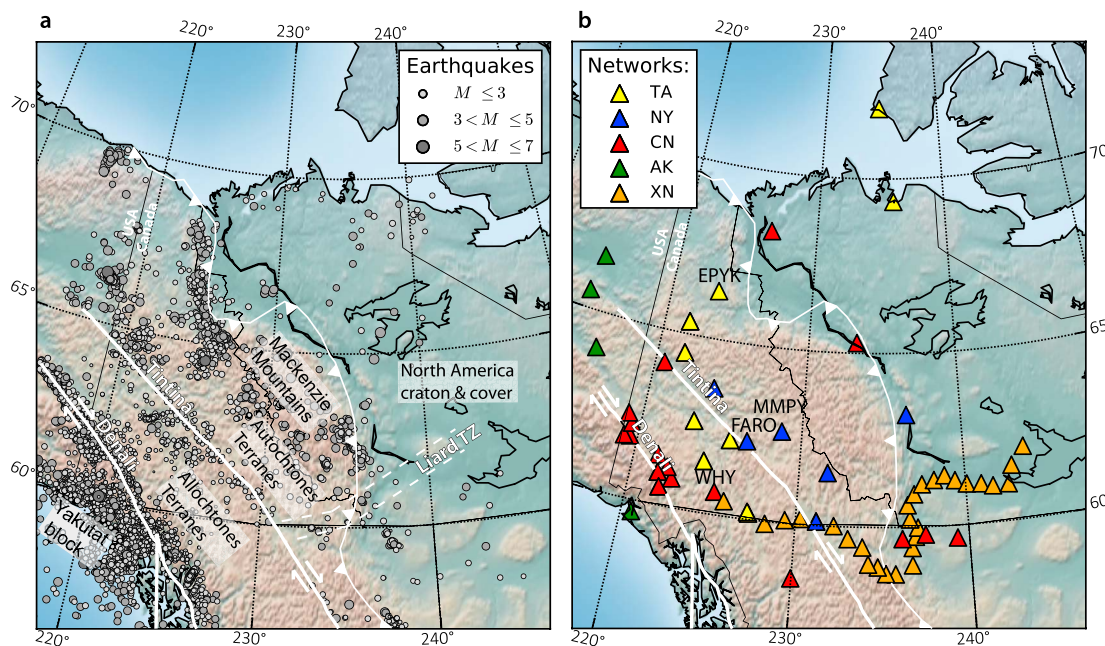


Figure 1. (a) Earthquake distribution (that occurred between 2000 and 2015, obtained from the Canadian National Earthquake Database—NEDB) and major tectonic boundaries in the northern Canadian Cordillera. The double arrows indicate the sense of shear on Denali and Tintina Faults. The curvy line with arrowheads shows the outline of the Cordilleran Deformation Front with main thrust faults dipping toward the Cordillera. Liard TZ: Liard transfer zone. (b) Broadband seismograph stations used in this study. Stations with labels are discussed in the text.

potential energy, boundary forces from relative plate motions, and basal tractions caused by mantle flow. Their results suggest that present-day deformation of the external domains (central, northern, and western parts of the Cordillera) result from a regional southward mantle flow deflected eastward into the northern Canadian Cordillera, with a flow rate decreasing toward the Cordilleran Deformation Front. This model predicts that stresses are propagated throughout the whole lithosphere, with strongly coupled upper crust, lower crust, and upper mantle, in apparent contradiction with the orogenic float model and thermal-rheological models of lithospheric strength.

Because both end-member models can explain the first-order patterns of surface deformation data (e.g., GPS), discriminating between them is contingent upon accurate structural information of the crust and uppermost mantle beneath the Cordillera. In particular, one of the key constraints is crustal thickness. Active source seismic studies carried out as part of Lithoprobe project [e.g., Clowes *et al.*, 2005] indicate that the crust is ~35 km thick along the seismic profiles, but spatial coverage is sparse. Additionally, important structural information can be obtained from estimates of seismic anisotropy. Within the orogenic float framework, shearing along a weak lower crustal detachment should impart a strong mineral fabric and give rise to elastic anisotropy, which can be deciphered using seismic data. However, there are currently few constraints on seismic anisotropy of the crust in the northern Canadian Cordillera [e.g., Rasendra *et al.*, 2014]. In addition, characterization of the anisotropy in the uppermost mantle beneath the Cordillera may help discriminate between small-scale convection, proposed as a mechanism for the orogenic float elevated geotherm [Currie and Hyndman, 2006], and large-scale mantle flow, resulting in crustal deformation [Finzel *et al.*, 2015] and elevated geotherm at the edge of the craton [e.g., Bao *et al.*, 2014].

In this study, we use scattered teleseismic P waves (i.e., receiver functions) to study both the structure and anisotropy of the crust and uppermost mantle in the northern Canadian Cordillera, in order to evaluate the validity of the proposed tectonic models. Receiver functions are sensitive to scale lengths of 1–10 km and are therefore ideal to resolve crust and mantle stratification. These new seismic data benefit from increased coverage of broadband seismic stations due to recent and ongoing deployments (e.g., Yukon-Northwest Seismograph Network; Transportable Array of USArray; Figure 1b), which dramatically improves the resolution and accuracy of seismic velocity models.

We first review the geology and tectonic setting of the area in section 2, followed by a description of the methodology employed to calculate receiver functions. After briefly describing observable features in receiver function data that offer some insight into the complexity of subsurface structure in section 3, we perform postprocessing of the receiver functions to extract meaningful structural information. We focus on three complementary approaches: $H\text{-}\kappa$ stacking to recover Moho depth in section 4, harmonic decomposition to visualize the seismic anisotropy signals as a function of depth in section 5, and forward modeling of receiver function data for selected stations in section 6 to provide semiquantitative estimates of structural properties, which can be extrapolated to other stations via their harmonic component signatures.

2. Tectonic Setting

The Canadian Cordillera is a Phanerozoic mountain belt that extends from the Canada-U.S. border in the south to the Beaufort Sea and Alaska in the north [Johnston, 2008]. Although the Cordillera has similar physiography along its length, there are different neotectonic regimes acting on this area mainly due to variations in plate tectonic interactions at its western margin [Mazzotti *et al.*, 2008]. The tectonic history of the Canadian Cordillera extends back around 750 Ma [e.g., Monger and Price, 2002; Nelson and Colpron, 2007], including the late Neoproterozoic-Early Cambrian breakup of Laurentia and formation of a passive margin that is preserved today within the eastern Canadian Cordillera, several subduction and collision episodes throughout the Mesozoic, major transpressive phases leading to the formation of the lithospheric-scale Tintina and Denali Fault systems during Late Cretaceous-Eocene, and recent terrane accretion and large-scale transpressive deformation. The Liard transfer zone (LTZ) is an important structural transition oriented approximately NE-SW inherited from the asymmetric rifted margin of Laurentia in the late Proterozoic [Hayward, 2015]. It marks the boundary between former footwall (to the north) and hanging wall (to the south) and separates the northern from the southern part of the Canadian Cordillera [Cecile *et al.*, 1997]. Figure 1a shows the main belts making up the northern Canadian Cordillera as a result of this complex evolution.

Contemporary tectonics of the northern Canadian Cordillera are dominated by the oblique collision of the Yakutat Block with North America, which has contributed to the building of the tallest mountains in North America (Fairweather and St-Elias-Chugach Mountains) [Mazzotti *et al.*, 2008]. According to seismicity and Global Positioning System (GPS) data, the collision of the Yakutat Block (circa 50 mm/yr) results in a complex partition of the deformation with significant shortening and lateral extrusion in southeastern Alaska, whereas southwestern Yukon is affected by the indentation effect of the collision syntaxis [e.g., Leonard *et al.*, 2008; Elliott *et al.*, 2013; Maréchal *et al.*, 2015]. The most recent GPS and tectonics data also suggest that strain transfer from the collision front to the Canadian Cordillera is probably significantly smaller than originally proposed in the orogenic float model, with very slow (1–2 mm/yr) transpressive motion along the Denali Fault in Yukon and only 1–2 mm/yr of eastward motion in the central Cordillera [e.g., Maréchal *et al.*, 2015].

3. Receiver Functions

3.1. Data Processing

We calculated receiver functions for 66 broadband seismograph stations located in northwestern Canada and eastern Alaska, in a region that stretches over 1600 km through the northern Canadian Cordillera and across the adjacent Canadian Shield (Figure 1b). Among these stations, 21 are from the permanent Canadian National Seismograph Network (CN; 17) and Alaska Regional Network (AK; 4) that have been continuously recording for several years up to over a decade. We used six stations of the Yukon-Northwest Seismograph Network (NY) installed in the summer of 2013 and nine stations from the Transportable Array (TA) network that started recording data in southwestern Yukon in the fall of 2015. These recent additions represent a twofold increase in the number of stations covering the northern Canadian Cordillera, but more importantly they fill a gap in the central portion of the Cordillera. We also included stations from the relatively densely spaced (average spacing of ~50 km), temporary Canadian Northwest Experiment deployment (CANOE, network code XN). These stations were in operation for 1.5 years on average between the summer of 2003 and the spring of 2005. We ignored stations located in the high-elevation St-Elias-Chugach region (south of the Denali Fault trace, Figure 1b) because we are mainly interested in the architecture of the crust and uppermost mantle away from the main plate boundary. Several stations are located in the thick sediment-filled foreland basin landward of the Cordilleran Deformation Front (Figure 1b). The reverberating

effects of the sedimentary layers may contaminate results for these stations, and we ignore the results for these stations.

Three-component seismograms are collected for all events with moment magnitude superior to 5.5 in the epicentral distance range 30°–90° that occurred between 2003 and 2016 (supporting information Figure S1). The back azimuth range between 120°W and 165°W is generally poorly sampled. For each event we use the velocity model iasp91 [Kennett and Engdahl, 1991] to extract 120 s windows centered on the predicted teleseismic P wave arrival time. The vertical and horizontal (radial and transverse) components of motion are decomposed into upgoing P , S_V (vertically polarized shear), and S_H (horizontally polarized shear) wave modes [Bostock, 1998] assuming a surface P wave velocity of 6.0 km/s and V_p/V_s of 1.75. We retain seismograms with P component signal-to-noise ratios superior to 5 dB over the first 30 s, measured in the 0.05–1 Hz frequency band. Individual single-event seismograms are processed using the receiver function method. We use the P component as an estimate of the source wavelet to deconvolve the S_V and S_H components using a modified Wiener spectral deconvolution, where the regularization parameter is calculated from the preevent, covariant noise spectrum between vertical and horizontal components to reduce contamination from seasonal noise effects [Audet, 2010]. Final receiver functions are filtered using a second-order Butterworth filter with corner frequencies of 0.05–0.5 Hz and are subsequently stacked into 10° back azimuth and 0.002 s/km slowness bins.

Receiver functions represent P -to- S converted signals generated from seismic velocity contrasts at depth and are typically used to map the crust-mantle boundary on continents [e.g., Xu *et al.*, 2007; Piana Agostinetti and Amato, 2009]. For simple continental structure (Moho depth < 50 km) the direct, primary P -to- S conversion (P_s) from the Moho interface generally arrives within 5 s of the direct P wave phase. Later arrivals are due to either deeper (i.e., upper mantle) interfaces or reverberations from free-surface reflections that generate secondary P -to- S conversions. These include the P_{ps} (or $PpPs$) and P_{ss} (or $PpSs + PsPs$) arrivals between 15 and 20 s following the direct P wave phase for a Moho depth of ~40 km. In general, the projection of signal onto the S_V and S_H components gives constraints on the structural complexity of the underlying medium. If the crust were uniform and isotropic with a flat Moho, part of the P wave would be converted onto the S_V component of motion but not onto the S_H component, for any back azimuth of incoming wave field. The absence of signal on the S_H component is therefore a clear indication of an isotropic medium containing only flat layers. In this case the amplitude of the S_V component would show an increase in P_s amplitude with increasing slowness (increasing angle of incidence or decreasing distance from the source). The presence of S_H energy and back azimuthal variations in S_V amplitude imply either structural heterogeneity (e.g., dipping interface or layer) or anisotropy, or both [Cassidy, 1992; Levin and Park, 1997; Savage, 1998; Frederiksen and Bostock, 2000; Audet, 2015].

It is typically very difficult to distinguish between the effects of dipping layers and anisotropy as they can produce similar patterns in both the S_V and S_H components [e.g., Porter *et al.*, 2011], except for special cases [Licciardi and Piana Agostinetti, 2016]. For models characterized by a dipping interface (or layer) with different velocities across it, or by a horizontal interface separating an isotropic medium from one characterized by hexagonal anisotropy with a dipping fast or slow axis of symmetry, we expect to see periodic variations in amplitude over 360° in back azimuth and a 90° shift between S_V and S_H amplitude patterns [Porter *et al.*, 2011; Bianchi *et al.*, 2010; Audet, 2015]. For anisotropy models with near-horizontal axis of hexagonal symmetry, the periodicity becomes 180°. Models with near-vertical axis of symmetry produce little variations in back azimuth due to poor sampling by steeply incident teleseismic P waves. For all other cases of anisotropy (e.g., lower order of elastic symmetry), the patterns can be much more complex. In any case, knowledge of the geology can help to distinguish between these scenarios.

3.2. Results

Figures 2–4 show radial and transverse component receiver functions for stations MMPY, WHY, and NBC3, respectively. These stations provide good examples of signal complexity in our data set. MMPY is located in the central part of the northern Canadian Cordillera, southwest of the Mackenzie Mountains and east of the Tintina Fault, whereas WHY is located in southwest Yukon between the Tintina and Denali Faults (Figure 1b). NBC3 is located to the east of the Cordilleran Deformation Front, on top of the thick foreland sedimentary basin (Figure 1b). Radial and transverse receiver functions are sorted by back azimuth and displayed over 30 s, which allows visualizing the direct crustal conversions and reverberations.

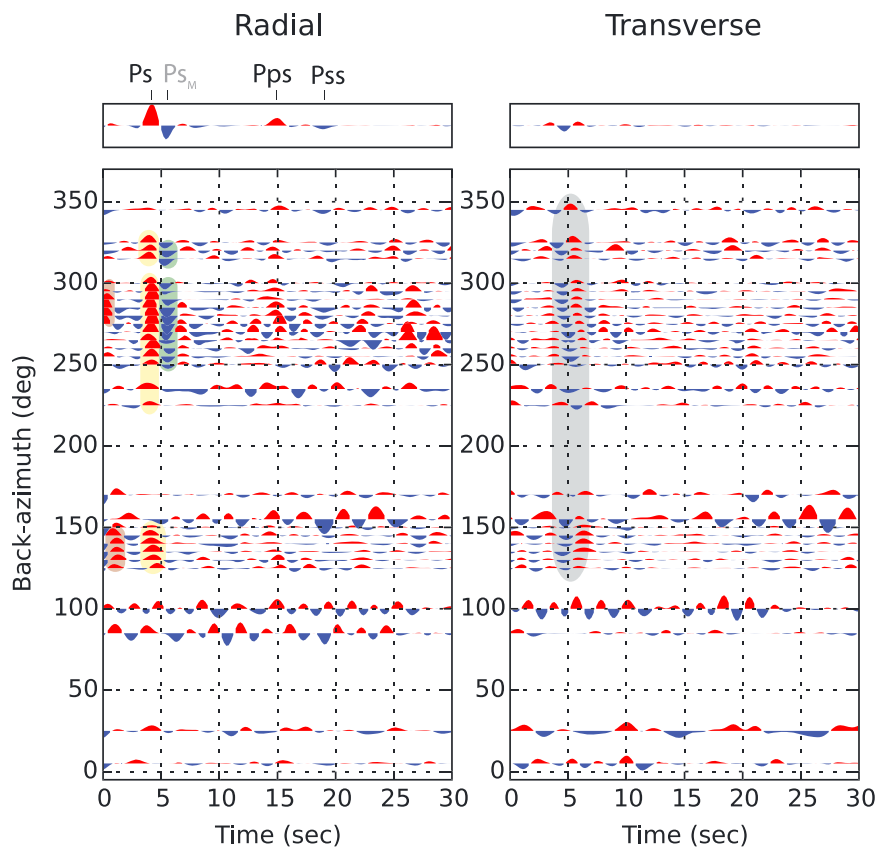


Figure 2. Receiver functions for station MMPY shown over 30 s. The (left) radial and (right) transverse components, sorted by back azimuth of incoming wave field within 5° bins. Slowness information is averaged out. The top traces show the receiver functions further averaged over all back azimuth and slowness values. The positive pulses at 4 and 15 s and negative pulse at ~ 18 s on the radial component are consistent with Ps , Pps , and Pss conversions at the Moho. The negative pulse at ~ 5.5 s (labeled Ps_M in gray) and corresponding signals on the transverse component indicate a negative velocity contrast at increasing depth immediately beneath the Moho. Back azimuth variations in the timing and amplitude of receiver function signals indicate seismic anisotropy. Shaded areas highlight signals discussed in the text.

Data recorded at station MMPY (Figure 2) show back azimuth variations in the amplitude and arrival time for both the radial and transverse components. The maximum positive amplitude on the radial component at roughly 4 s is interpreted as the direct Ps conversion from a downward seismic velocity increase associated with the Moho, with a corresponding low-amplitude, positive Pps arrival at ~ 15 s and a faint negative Pss arrival at 18–20 s. The negative pulse at ~ 5.5 s could represent a slightly deeper interface with a downward decrease in seismic velocity, suggesting the presence of a high-velocity layer beneath the Moho. There is also an indication for a shallow interface in the crust shown by the low-amplitude positive pulses at ~ 0.5 –1.5 s. In addition, variations in the timing and amplitude of signal with back azimuth on both the radial and transverse components indicate pervasive directional structure (either dipping interface or anisotropy). The early positive arrival is maximum at back azimuths $\sim 130^\circ$ – 150° (at 1.5 s) and $\sim 270^\circ$ – 300° (at ~ 0.5 s), suggesting anisotropy in the shallow crust. The Moho signal and the associated negative arrival at ~ 5.5 s both display maximum amplitude at back azimuth $\sim 270^\circ$ on the radial component, whereas the transverse component shows large moveout with back azimuth and a change in polarity.

Receiver functions for station WHY (Figure 3) show similar patterns: positive Ps signals at ~ 1 s and ~ 4 s from upper crustal and Moho discontinuities, respectively, and a negative arrival at ~ 5.5 s, presumably from a sub-Moho discontinuity with a downward negative impedance contrast. The positive Pps and negative Pss signals associated with the Moho are less visible on the stacks of the radial component (expected at ~ 15 and ~ 20 s), possibly due to interference with Ps arrivals from deeper seismic discontinuities or from the scattering effect of topography and relief on free-surface reverberations. Directional variations in receiver function amplitudes are also visible on both the radial and transverse components, with higher amplitudes compared with those

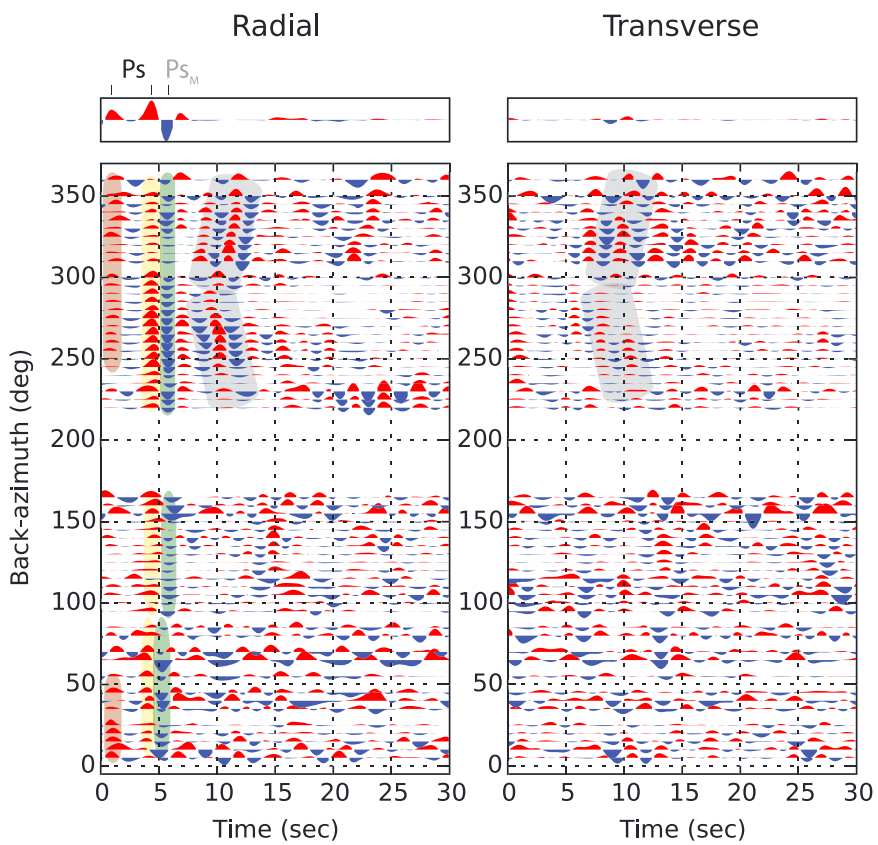


Figure 3. Receiver functions for station WHY. Figure format is the same as in Figure 2. The positive signal at ~ 1 s and ~ 4 s on the radial component are consistent with P_s arrivals from a shallow crustal interface and the Moho. The free-surface reverberations are not evident from these data. The negative pulse at ~ 5.5 s (labeled P_{sM}) is consistent with similar signal observed at station MMPY. The later arrivals (between 7 and 13 s) exhibit strong seismic anisotropy and indicate complex sub-Moho structure beneath station WHY. Shaded areas highlight signals discussed in the text.

observed at MMPY. For example, the positive-negative signals at ~ 4 – 6 s on the radial component are strongest at back azimuth ~ 250 – 260° . Between 7 and 13 s, high-amplitude scattering with directional moveout and polarity changes are observed on both the radial and transverse components within the back azimuth range $\sim 240^\circ$ – 360° . An interesting polarity reversal occurs simultaneously on both components at back azimuth $\sim 300^\circ$, which is difficult to reconcile with simple heterogeneity (i.e., dipping layer) or hexagonal anisotropy and suggest a relatively small anisotropic volume sampled by these data. These observations suggest that signals from deep (i.e., upper mantle) and shallow (i.e., crustal) structure may be tangled up and can be difficult to distinguish from visual inspection.

Receiver functions for station NBC3 (Figure 4) are visibly different. The positive pulse with maximum amplitude arrives at ~ 1 – 2 s and does not coincide with the expected Moho arrival. The early arrivals alternate between strong positive and negative pulses that are typical of reverberations originating from a thick and shallow, low-velocity sedimentary basin [Frederiksen and Delaney, 2015], which completely mask the Moho signals. Although the azimuthal coverage is not optimal, the presence of anisotropy is visible between 4 and 6 s as polarity reversals on the radial component. The scattering appears much stronger on the radial component for events with back azimuths between 90° and 180° . Transverse component signals are largely incoherent.

3.3. Moho Sharpness and Layering

The sharpness of the Moho provides important constraints on the processes that control lithospheric evolution [Levin et al., 2016]. A simple way to characterize Moho sharpness is by looking at the variations in the shape of the Moho signal at increasing frequency. A vertical step change in seismic property yields a pulse with progressively decreasing width with increasing frequency (i.e., property of a delta function). The frequency at which the

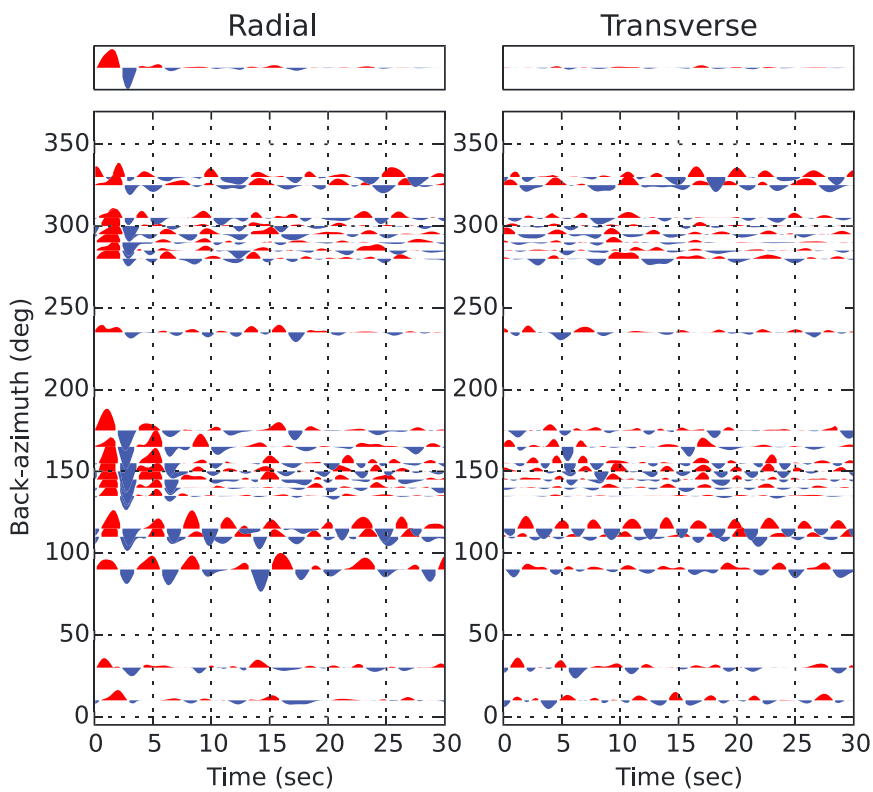


Figure 4. Receiver functions for station NBC3. Figure format is the same as Figure 2. Here the sequence of positive and negative pulses is characteristic of reverberations from a near-surface low-velocity layer, such as the deep foreland sedimentary basin adjacent to the Cordilleran Deformation Front to the east of the northern Canadian Cordillera. None of these signals can be identified with P_s , P_{ps} , and P_{ss} arrivals from the Moho.

pulse width stops decreasing can be used to characterize the width of a vertical velocity gradient, whereas layering will produce distinct pulses at increasing frequency. Figure 5 shows stacks of radial receiver functions at four stations (MMPY, WHY, FARO, and EPYK) and sorted by increasing high corner frequency

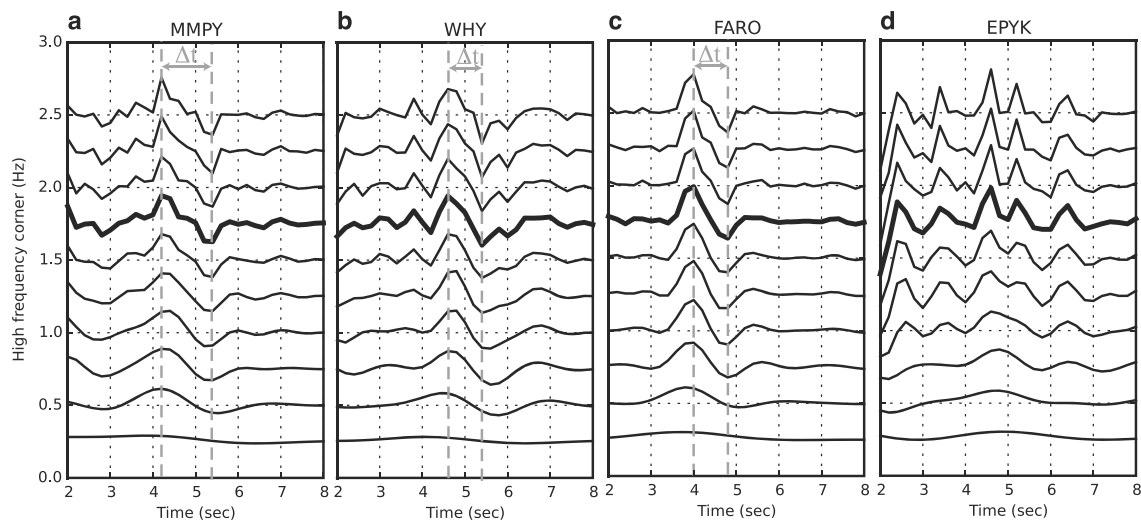


Figure 5. Stacks of radial components sorted by increasing high-frequency corner of the band-pass filter for stations (a) MMPY, (b) WHY, (c) FARO, and (d) EPYK. The stacks are windowed between 2 and 8 s to encompass the P_s Moho arrival, represented by the highest positive pulse between 4 and 4.5 s in all cases. Vertical dashed lines show the time difference (~ 1 s) between the Moho pulse and the largest negative arrival, which indicates a sub-Moho discontinuity with a downward negative velocity contrast (i.e., sub-Moho high-velocity layer). The traces with thick black lines indicate (approximately) the frequency at which the width of the Moho pulse stops changing.

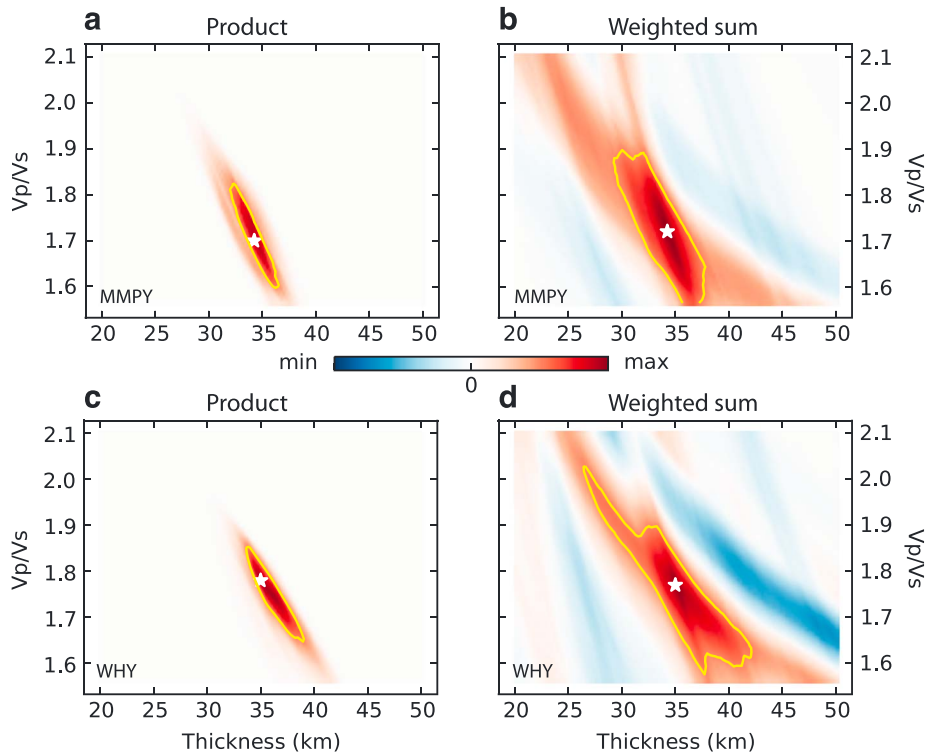


Figure 6. $H\text{-}\kappa$ stacks for stations (a, b) MMPY and (c, d) WHY obtained using the product (Figures 6a and 6c) or weighted sum (Figures 6b and 6d) of individual phase stacks. Negative amplitudes are absent from Figures 6a and 6c. The yellow contours show the error estimates, and the white stars show the location of the maximum stack amplitude.

of the band pass filter. The stacks are windowed between 2 and 8 s to encompass the P_s conversion from the Moho. The maximum frequency at which the pulse size stops decreasing is ~ 1.75 Hz for all stations; this result is typical of Moho signals over the entire network. These frequencies correspond to shear wavelengths of ~ 2.1 km, resulting in a maximum vertical extent over which seismic properties change at the Moho of $\sim 1\text{--}2$ km [Levin *et al.*, 2016], thus indicating a seismically sharp Moho.

Stations MMPY, WHY, and FARO also display a negative arrival around ~ 1 s following the positive Moho arrival, as outlined previously. The two separate arrivals are more visible, and the time separation is better constrained at frequencies above 1.75 Hz, which allows us to estimate the thickness of a high-velocity layer immediately beneath the Moho. The time separation between two vertically propagating P -to- S converted waves from horizontal boundaries separated by h is $\Delta t = \frac{h}{V_s} - \frac{h}{V_p} = \frac{h}{V_s} \left(\frac{\alpha-1}{\alpha} \right)$ where $\alpha = \frac{V_p}{V_s}$ within the sub-Moho layer. Assuming seismic velocities of uppermost mantle lithosphere within the layer ($V_s = 4.3$ km/s, $V_p = 7.8$ km/s), we obtain $h \approx 10$ km. Stations WHY and EPYK display additional positive pulses at frequencies > 1 Hz, indicating a more complex layered structure around the Moho as compared with stations MMPY and FARO.

4. $H\text{-}\kappa$ Stacking

4.1. Processing

The $H\text{-}\kappa$ stacking technique developed by Zhu and Kanamori [2000] provides point estimates of Moho depth (H) and bulk crustal V_p/V_s (κ) beneath each station. The procedure is based on stacking the amplitude of moveout-corrected traces for S_V converted phases (P_s , P_{ps} , and P_{ss}) in the receiver functions for a given model and searching through a range of parameters for the model that maximizes the weighted sum of the phase stacks. This is expressed as

$$A_S(H, \kappa) = w_1 P_s(H, \kappa) + w_2 P_{ps}(H, \kappa) + w_3 P_{ss}(H, \kappa), \quad (1)$$

where A_S is the weighted sum and w_i are the arbitrary weights. This method works well for layered, isotropic media where the Moho is flat and lithospheric structure is simple. In the Cordillera, the Moho signals, in

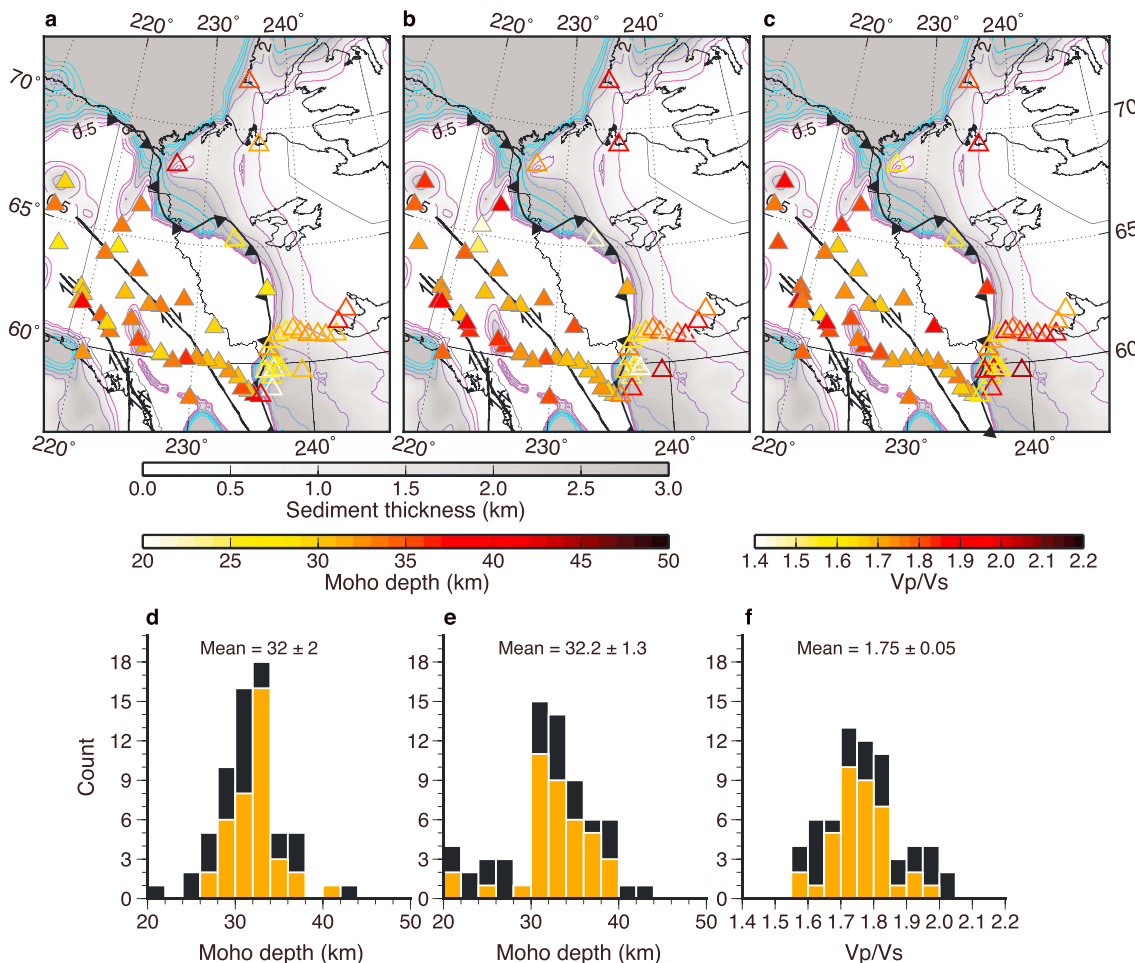


Figure 7. Results of Moho depth and V_p/V_s obtained from receiver functions. Maps of Moho depth obtained (a) from the $H\text{-}\kappa$ stacking technique and (b) from assuming a fixed, uniform V_p/V_s value of 1.73. The maps are generally consistent with each other and show overall low (<40 km) values, except where sediment thickness is high (>1 km). (c) Map of V_p/V_s values obtained from the $H\text{-}\kappa$ stacking technique. Solid and empty triangles show stations located within and outside of the region with no sediments, respectively, roughly following the Cordilleran Deformation Front. Histograms of (d, e) Moho depth and (f) V_p/V_s calculated for all stations (black bars) and those within the region with no sediments (orange), for the corresponding maps in Figures 7a and 7c, with mean and standard deviation. Sediment thickness data are from Mooney and Kaban [2010].

particular the free-surface reverberations, can be disrupted or masked by arrivals from shallower or deeper interfaces or anisotropy (e.g., Figure 5) or may suffer from topographic scattering effects.

We therefore modify the $H\text{-}\kappa$ stacking technique to mitigate some of the problems associated with complicated signals, as follows: Prior to creating individual phase stacks, we filter direct conversions at higher frequencies (0.1–0.5 Hz) than reverberations (0.1–0.35 Hz) [e.g., Audet *et al.*, 2010]. We use the technique of Schimmel and Paulsen [1997] for stacking individual moveout-corrected phases to improve stack coherency. After constructing each phase stack for Ps , Pps , and Pss , we keep amplitude information that matches the polarity expected for conversions caused by a downward velocity increase at the Moho. This involves setting to 0 negative amplitudes in the Ps and Pps stacks and positive amplitudes in the Pss stack. We then multiply the phase stacks (reversing the sign of the Pss stack) instead of performing a weighted sum and obtain a more coherent final stack that contains minimal interference from undesired arrivals. Mathematically, this can be expressed as

$$A_M(H, \kappa) = Ps^+(H, \kappa) \cdot Pps^+(H, \kappa) \cdot (-Pss^-(H, \kappa)), \quad (2)$$

where A_M is the resulting product, and the superscripts (+ or -) denote the sign of amplitudes kept in each phase stack. Examples for stations MMPY and WHY and a comparison with the standard, weighted sum method are provided as supporting information (Figures S2–S5).

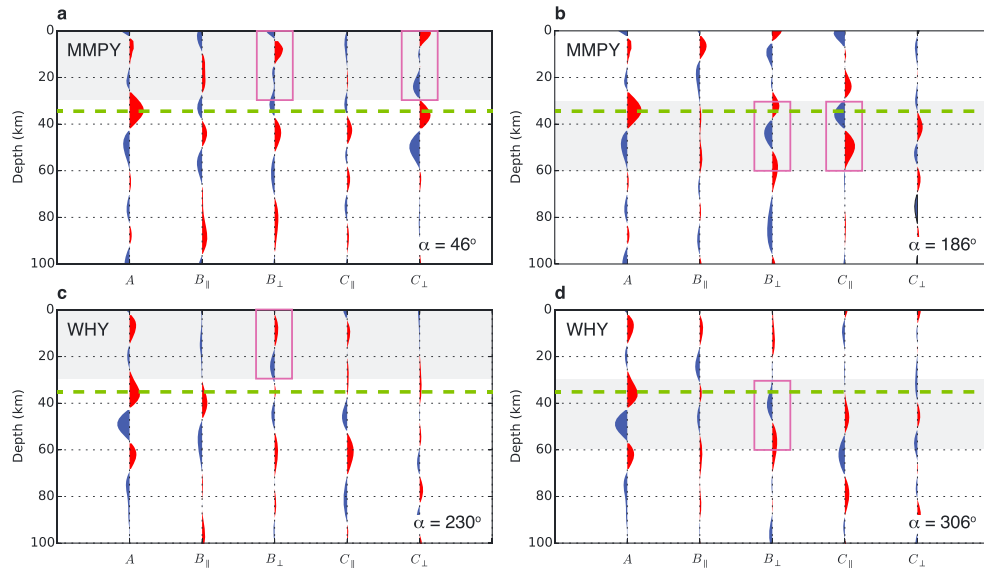


Figure 8. Results of the harmonic decomposition for stations (a, b) MMPY and (c, d) WHY. For each station, decomposition is performed by minimizing the signal on component B_{\parallel} within a depth interval shown in gray. Moho depth is indicated by the green dashed horizontal line. The estimated azimuth α is displayed to the bottom right of each panel. The magenta boxes indicate features of interest that are discussed in the text.

We use a one-dimensional seismic velocity model containing a single, uniform crustal layer over a mantle half space with crustal P wave velocity of 6.0 km/s to compute traveltimes from analytical solutions, although the results are only weakly sensitive to variations in P wave velocity [Zandt and Ammon, 1995]. Because data quality is variable within the network, we generally use a combination of two to three phases (Ps with either Pps and/or Pss) depending on the quality of the stacks and our ability to identify each scattered phase separately in the receiver function data. Since we use multiplication instead of averaging, we do not need to weigh phase stacks individually. Uncertainties in Moho depth and V_p/V_s values are estimated from the flatness of the stack around the solution [Zhu and Kanamori, 2000] and are defined by the 0.5 contour of normalized stack amplitude. Analysis of formal errors ($1 - \sigma$) based on the bootstrap method gives similar estimates.

4.2. Results

Figure 6 shows the final stacks for stations MMPY and WHY obtained using the standard weighted sum and the product of the cleaned stacks. For the standard application, we use weights of 0.5, 2, and -1 for the Ps , Pps , and Pss phase stacks, respectively, for station MMPY, and weights of 0.2, 2, and -1 for station WHY. The different choice of weights for Ps reflects the need to amplify the much weaker reverberated phases (Pps and Pss) for station WHY; otherwise, the final stack is dominated by the Ps stack and does not yield a clear maximum. The modified method produces a much cleaner final stack and more precise estimates. Visual inspection of these plots indicates similar estimates of $H\text{-}\kappa$ parameters for both techniques but much higher uncertainties using the standard approach. However, for stations on top of thick sedimentary layers, both $H\text{-}\kappa$ stacking techniques may still produce erroneous results (cf. Figures S6 and S7 where a clear Ps phase cannot be identified at the presumed Moho depth).

To evaluate the sensitivity of Moho depth to the estimated V_p/V_s , we also measured Moho depth by assuming a uniform V_p/V_s of 1.73 for all stations in the network and using only the Ps information, which is the best resolved and least ambiguous phase in receiver function data. We therefore produced two maps of Moho depth that are shown in Figures 7a and 7b. Due to the contaminating effect of shallow, thick (i.e., 1–10 km), and low-velocity sedimentary layers on the recovery of crustal parameters from receiver functions, we discard all stations located in regions where sediment thickness is >1 km, which are mainly located in the foreland basin to the east of the Cordilleran Deformation Front. Figures 7d and 7e show histograms of the recovered Moho depth values for the entire network (black) and for stations located in the northern Cordillera (orange), for both the variable and fixed V_p/V_s estimates. We find a

consistent mean Moho depth of 32 km and standard deviation of 2 km, similar to but somewhat lower than previous estimates [e.g., Kao *et al.*, 2013].

Figures 7c and 7f show a map and histogram of V_p/V_s values for the network and the subset of selected stations in the northern Cordillera. The V_p/V_s distribution gives a mean value of 1.75 and standard deviation of 0.1. From here on we will ignore data and results for stations located on top of the sedimentary basin with thickness > 1 km. Table S1 lists the individual $H\text{-}\kappa$ results for the stations located within the northern Cordillera.

5. Harmonic Decomposition

To better visualize crustal and uppermost mantle structure beneath individual stations, receiver functions are decomposed into back azimuth harmonics, a technique proposed by Bianchi *et al.* [2010] and slightly modified by Audet [2015].

5.1. Processing

Before performing the decomposition, we map S_V and S_H receiver functions from time to depth using the crustal P wave velocity model LITH5.0 [Perry *et al.*, 2002], which is a low-resolution compilation of seismic velocities based on Lithoprobe data. We set S wave velocities using a V_p/V_s of 1.75, but note that the crustal seismic velocity model only has a weak influence on the results. For the decomposition we assume that at every depth interval, the S_V and S_H receiver function amplitudes can be expressed as a sum of $\cos(k\varphi)$ and $\sin(k\varphi)$, where k is the harmonic degree and φ is the back azimuth. We limit our analysis to the first three harmonic degrees ($k = 0, 1, 2$), resulting in five harmonic components. The first term A , corresponding to $k = 0$, represents the mean amplitude of the radial component of the receiver functions over all back azimuths. This term contains information on the isotropic background velocity structure of the medium, with possible secondary effects from anisotropy or structural heterogeneity superimposed. $B_{||}$ and B_{\perp} are the terms for $k = 1$ presenting a periodicity of 360° in back azimuth. They are mainly sensitive to the presence of a dipping interface or anisotropic layering with a plunging fast or slow symmetry axis [Piana Agostinetti *et al.*, 2011; Audet, 2015]. The last two terms $C_{||}$ and C_{\perp} are for $k = 2$ presenting a periodicity of 180° . They indicate a structure characterized by an anisotropic layer with a dominantly horizontal symmetry axis [Shiomi and Park, 2008; Bianchi *et al.*, 2010; Audet, 2015; Cossette *et al.*, 2016]. A medium characterized by a vertical axis of hexagonal symmetry will not produce signal on the $k = 1$ and 2 components.

Using this construction, the coordinate system defined by zero-phase sine and cosine functions is aligned with the N-S and E-W geographic axes [Bianchi *et al.*, 2010]. This implies that structures (e.g., dipping interface) with a dominant N-S or E-W orientation generate S_V and S_H signals whose amplitude variations with back azimuth are fully mapped onto one of the two $k = 1$ components (i.e., the complementary $k = 1$ component contains no signal). In contrast, dipping structures or anisotropy with a dominant orientation oblique to the N-S/E-W frame of reference generates S_V and S_H signals that are projected onto both $k = 1$ components. Thus, we can determine the optimal orientation of the coordinate system that coincides with the dominant orientation of structure by minimizing the energy on a particular $k = 1$ component over a certain depth range, under rotation of the frame of reference. This step introduces an additional azimuth parameter α , which corresponds to the nonzero phase of the sine and cosine functions [Audet, 2015; Cossette *et al.*, 2016]. In this study we minimize the energy on $B_{||}$; thus, the resolved orientation α is aligned with either the strike of a dipping interface or the fast axis of hexagonal symmetry [Audet, 2015; Cossette *et al.*, 2016].

Based on receiver function data (sections 3.2 and 4.2), we define two distinct depth ranges: 0 to 30 km (roughly the surface to Moho depth) and 30 to 60 km (mostly the lithospheric mantle). This procedure hampers our ability to characterize intracrustal and sublithospheric variations in the orientation of anisotropy, and the recovered azimuth therefore represents the orientation of the dominant source of anisotropy within each depth range.

5.2. Results

Figure 8 shows example results of harmonic decomposition for stations MMPY and WHY. The signal on the A component correspond to the stack on the radial component of the receiver function (Figures 2 and 3) and does not depend on the selected depth interval. The Moho depths shown by the largest positive pulse on the A components coincide with those obtained with the $H\text{-}\kappa$ method for these stations. For station MMPY, the

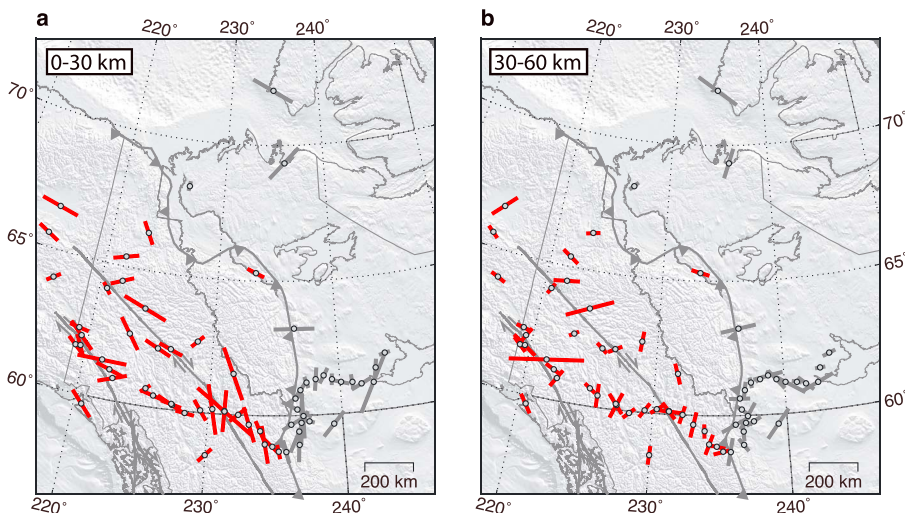


Figure 9. Maps showing the recovered α values representing the surface projection of the seismic fast axis, estimated for the (a) shallow (0–30 km) and (b) deep (30–60 km) intervals. Bar length is proportional to the variance of the B_{\perp} component within the corresponding depth range. Red and gray bars indicate results for stations located within the Cordillera and above the thick sedimentary basin, respectively; the latter results are ignored in the discussion.

azimuths α of the shallow and deep intervals are estimated at 46° and 186° , respectively. The difference in α between shallow and deep structures results in very different $k = 1$ and 2 harmonic components, with significant minimization of energy on the B_{\parallel} component at the corresponding depths (Figures 8a and 8b): For the crust interval, the B_{\perp} and C_{\perp} components show large positive pulses at ~ 8 – 10 km and ~ 5 km, respectively; for the mantle interval, large positive-negative pulses are found between 30 and 60 km on the B_{\perp} and C_{\parallel} components. The strong amplitude on the $k = 2$ component suggests that the sub-Moho layer is elastically anisotropic (as opposed to reflecting dipping structure) and that the plunge of the symmetry axis is low (near-horizontal axis). These results indicate directional structures with different orientation in the shallow upper crust and below the Moho.

In contrast, the harmonic components for station WHY indicate a dominantly isotropic crustal layer, as shown by the weak amplitude signal on the $k = 1, 2$ terms (Figures 8c and 8d). The azimuths α from the shallow and deep intervals are estimated at 230° and 306° , respectively, again reflecting shallow and deep structure with different directionality. Interestingly, the various harmonic components estimated for the deep interval show only modest amplitudes, in contrast to receiver function data described in section 3.2. This may reflect the large directional moveout that interferes destructively and decreases the amplitude of the harmonic terms. Nevertheless, the signals on the B_{\perp} and C_{\parallel} components are roughly similar to that observed for MMPY, indicating similar sub-Moho structure.

The azimuths α at both depth ranges estimated from the harmonic decomposition for all stations are shown in Figure 9, with the length of the bars proportional to the variance of the signal on the B_{\perp} component. To a first order, the Cordillera is characterized by a NW-SE orientation of α in the shallow (crust) depth range, roughly parallel to the Tintina and Denali Faults, whereas orientations of sub-Moho structures vary more largely between NE-SW and NW-SE.

5.3. CANOE Profile

Figure 10 shows the harmonic decomposition for stations along the CANOE line that follows the southern limit of the northern Cordillera (see Figure S8 for a complementary SW-NE profile). We select stations located at a maximum orthogonal distance of 100 km from the line in order to avoid distortion caused by possible 3-D structure. Since the parameter α changes along the line and for the two depth intervals (cf. Figure 9), we cannot set a decomposition that optimizes the signal on one of the $k = 1$ components for all stations. Instead, we perform the harmonic decomposition using $\alpha = 0$ for all stations, thereby letting the directional variability express itself as lateral variations in both $k = 1$ (and $k = 2$) components. In this case the B_{\parallel} and B_{\perp} components represent signal projected onto the N-S and E-W directions, respectively.

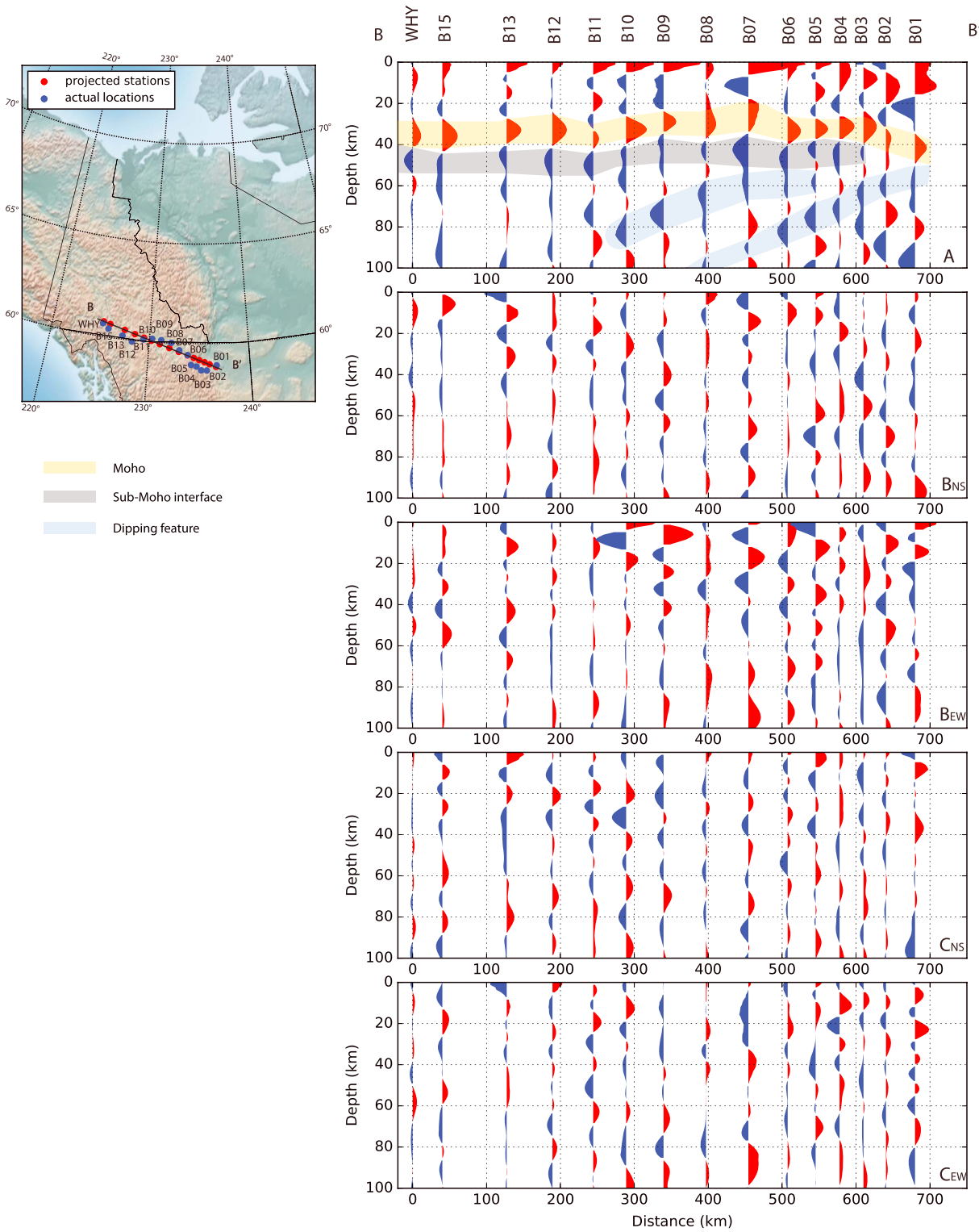


Figure 10. Profile showing the five harmonic components calculated with $\alpha = 0^\circ$ along line B-B', with possible interpretation. Stations from the CANOE network are projected along the line to avoid 3-D distortions. Most of the stations are within 50 km. All harmonic components are rotated to the NS and EW reference frame ($\alpha = 0$).

The Moho signal is clearly expressed at a depth varying between 30 and 35 km, with slight variations along the profile (component A). Signals from shallow discontinuities appear more prominently toward the eastern part of the profile and are associated with an apparent deepening of the Moho and the appearance of

Table 1. Seismic Velocity Models Used to Calculate Synthetic Receiver Functions for Stations MMPY and WHY^a

Station	Thickness (km)	Density (kg/m ³)	V_p (km/s)	V_s (km/s)	Anisotropy (%)	Trend (deg)	Plunge (deg)
MMPY	8	2700	5.5	3.16	-5	136°	50°
	26.25	2800	6.3	3.62	-	-	-
	10	3200	8.0	4.40	12	186°	10°
	Half space	3200	7.8	4.30	-	-	-
WHY	8	2700	5.5	3.10	-	-	-
	27	2800	6.3	3.54	-	-	-
	10	3200	8.0	4.40	12	216°	5°
	Half space	3200	7.8	4.30	-	-	-

^aCrustal thickness and P-to-S velocity ratio in the crust are taken to match the results obtained from the $H\text{-}\kappa$ stacking technique (Table S1). A negative/positive percent anisotropy implies a slow/fast axis of hexagonal symmetry oriented along trend (clockwise from north) and plunge (downward from horizontal) directions.

sedimentary layer signatures (stations B01–B03). Below the Moho, pervasive negative pulses indicate the presence of the negative velocity contrast at ~40–45 km, as well as a number of coherent but low-amplitude negative pulses associated with negative velocity contrasts dipping toward the west. The sub-Moho layer, observed in the receiver functions for individual stations (Figures 2, 3, and 5), appears continuous along the profile.

On the $k = 1$ and 2 harmonics, the signals do not appear as coherent. The dominant signals are observed on the B_{\perp} component, but the shape and polarity of the corresponding pulses are highly variable and do not show a consistent pattern. Anisotropy is disparate along the line: some stations show no or little anisotropy (e.g., station B12); others have more anisotropy either in the crust (e.g., station B10) or in the sub-Moho layer (e.g., station WHY). Overall, the anisotropy is more pronounced in the upper half part of the crust. There is strong amplitude on the $k = 2$ terms with coherent smaller scale patterns, which can be observed at shallow depth, however at much lower amplitude.

6. Modeling

The harmonic decompositions demonstrate the complexity in subsurface structure but provide limited insight into quantitative models of crust and upper mantle properties. In this section we provide first-order, semiquantitative constraints on the seismic velocity structure and anisotropy of the crust and upper mantle by modeling synthetic receiver functions. The goal is to construct the simplest seismic velocity model consistent with observed data, whose harmonic component signature can then be extrapolated to other stations within the network. The seismic velocity models incorporate estimates of crustal properties determined in previous sections, adding complexity (sub-Moho layer, anisotropy) that matches the harmonic components from both observed and synthetic data.

We generate synthetic receiver functions by modeling plane wave propagation through a stack of homogeneous, anisotropic and flat layers using the reflectivity technique of Kennett [1983] and Thomson [1996], in a manner similar to Cossette *et al.* [2016]. The seismic velocity models are constructed from any number of isotropic or anisotropic layers. Each isotropic layer is characterized by four values: thickness, density, and P and S wave velocities. We model seismic anisotropy with either a fast or slow axis of hexagonal symmetry. The anisotropy is parameterized by the percent anisotropy and the trend and plunge of the symmetry axis, for a total of seven parameters for the layer. Synthetic receiver functions are generated at the same back azimuth and slowness range as the observed data and are also postprocessed using the harmonic decomposition technique.

The number of parameters to explore increases rapidly with the number of layers and the inclusion of anisotropy. The results are inherently nonunique due to incomplete and biased sampling of the subsurface by receiver function data. Therefore, instead of performing a Monte Carlo style parameter search, we build our models incrementally based on the simplest structure that can explain the data: first Moho depth and crustal V_p/V_s values are extracted from the $H\text{-}\kappa$ results to produce the simplest structure that reproduces the main receiver function signals; then we use the harmonic components to guide the construction of more complex subsurface models by adding layers or anisotropy, while keeping Moho depth and crustal V_p/V_s values fixed.

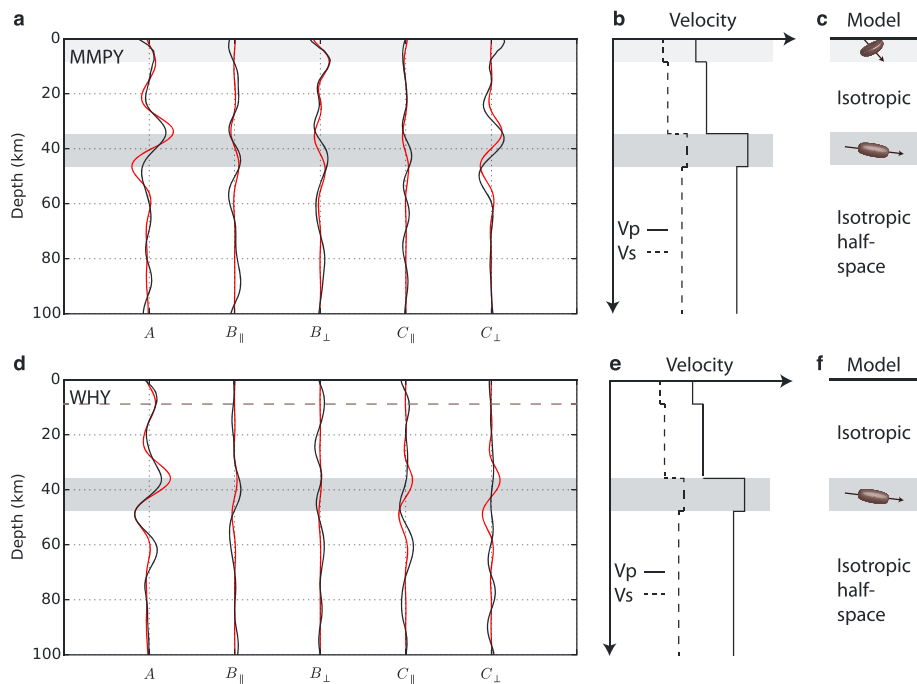


Figure 11. Results of synthetic receiver function modeling for stations (a–c) MMPY and (d–f) WHY. In Figures 11a and 11d the synthetic (red) and observed (black) receiver functions are represented by their harmonic components, calculated for $\alpha = 46^\circ$ (Figure 11a) and $\alpha = 230^\circ$ (Figure 11d). Seismic velocity models are shown in Figures 11b and 11e (see Table 1 for details). Figures 11c and 11f show the nature of each layer, where shaded areas (corresponding to those in Figures 11a, 11b, 11d, and 11e) indicate anisotropic layers, with either a slow (light gray) or fast (darker gray) axis of hexagonal symmetry as indicated by the arrows and symbols.

We model receiver function data for stations WHY and MMPY, since they are unaffected by sediments and are representative of data complexity observed in the network. The final velocity models and synthetic receiver functions (compared to the observed ones) are shown in Table 1 and Figure 11 (cf. also Figures S9 and S10). Both the synthetic receiver functions and the associated harmonic components appear to match the observed data reasonably well, although the latter contain additional signals that are not captured by our simple model, especially for station WHY, consistent with receiver function complexity observed previously (Figure 3). Nevertheless, this simple approach shows that receiver function data are consistent with a thin (~ 8 km) and variably anisotropic upper crustal layer, as well as a ~ 10 km sub-Moho high-velocity anisotropic layer characterized by a low-plunging fast axis of hexagonal symmetry.

7. Discussion

7.1. Crustal Structure

Our results indicate that the Moho is sharp and relatively flat with an average depth of 32 ± 2 km depending on the crustal V_p/V_s value (Figure 7). The Moho depths imaged using the harmonic decomposition (Figure 8) are consistent with these results and also agree with Moho values of 30–35 km found in previous seismic studies [e.g., Lowe and Cassidy, 1995; Clowes et al., 2005; Calvert, 2016]. The Moho depth apparently increases toward the Cordilleran Deformation Front to the southeast of the study area (Figure 12). The flatness and sharpness of the Moho signature are consistent with the removal of crustal roots and Moho topography from past tectonic events by lower crustal shearing or delamination, both requiring a hot geotherm over the whole Cordillera [Hyndman and Currie, 2011].

Spatial variations in crustal properties are shown by the variability of the V_p/V_s ratio and, mostly, of seismic anisotropy. The mean V_p/V_s ratio is 1.75 with a standard error on the mean of 0.05 (Figure 9), within a range of typical values for the crust [Zandt and Ammon, 1995]. Variations at short spatial scales likely indicate strong heterogeneity in the composition of the Cordilleran crust. The receiver function data display a shallow interface at ~ 8 –10 km depth (Figures 2 and 3) that is not continuous along the southern profile and with a

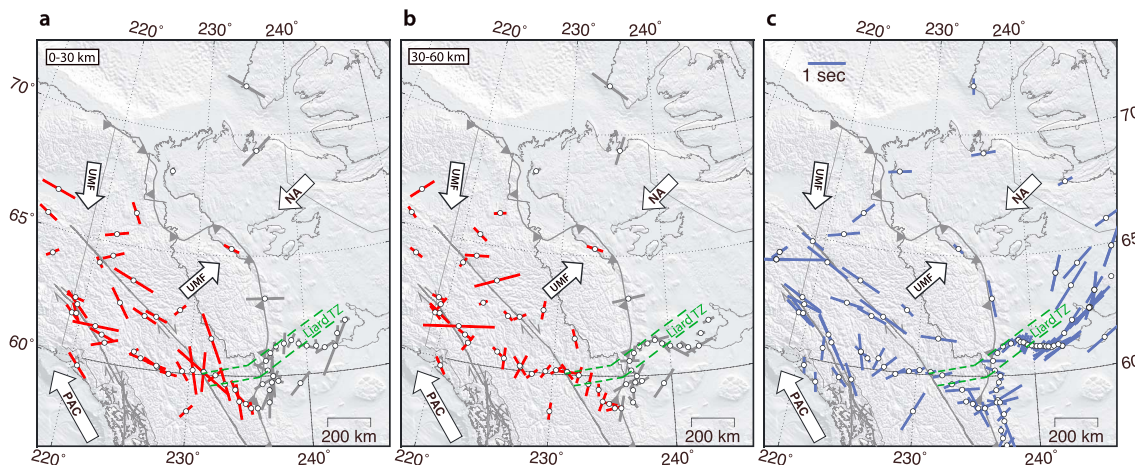


Figure 12. (a, b) Orientation of seismic fast axis estimated with RFs (this study) and (c) teleseismic shear wave splitting compiled in Audet *et al.* [2016, and references therein]. Arrows showing the motion directions of upper mantle flow (UMF) as proposed by Finzel *et al.* [2014] and of the North America (NA) plates and the Pacific (PAC) plates. Liard TZ: Liard transfer zone; see text.

stronger signal toward the Cordilleran Deformation Front (Figure 10). The harmonic decomposition of the receiver functions highlights a significant anisotropy in the crust, principally in the upper 10–15 km (Figures 9–11). Although the fast axis azimuths are, to a first order, generally oriented NW–SE, significant spatial variations exist in the amplitude and direction of the anisotropy (Figures 9 and 10), consistent with the much more spatially limited study of Rasendra *et al.* [2014]. The source of this anisotropy could be due to the presence of fractures in the upper crust or mica-rich mylonites around faults, although we cannot rule out the presence of dipping structures that could give rise to similar signals. Regardless of its origin, the overall anisotropy direction is consistent with the trends of the Tintina and Denali Faults and with the overall structural grain of the Cordillera terranes, potentially reflecting the effect of lateral amalgamation of crustal material during convergence, as inferred from previous active and passive seismic studies [Clowes *et al.*, 2005; Rasendra *et al.*, 2014; Calvert, 2016].

7.2. Uppermost Mantle Structure

We find a sub-Moho interface characterized by a negative pulse with a high amplitude at ~5.5 s on the receiver functions (Figures 2, 3, and 5), suggesting that this layer has a high seismic velocity relative to that of the underlying uppermost mantle. The thickness of the high-velocity, sub-Moho layer is estimated at around 10 km (Figures 5 and 11). This structure is found all along the southern profile (Figure 10) at roughly 40–45 km depth and is probably present over the entire northern Cordillera. This layer is also characterized by strong anisotropy, indicated by a clear delay time and change in polarity on the transverse component of the receiver functions. The anisotropy orientation for the 30–60 km deep range that encompasses this layer is roughly NE–SW in the central Cordillera and almost N–S toward the Yukon–BC border. The signals associated with the sub-Moho layer are consistent with anisotropy due to a low-dipping fast axis of hexagonal symmetry (Figure 11).

The high-velocity nature of the sub-Moho layer is puzzling as it is inconsistent with low Pn velocities estimated using active source refraction data [Clowes *et al.*, 2005]. Although unlikely, the low observed Pn velocities may reflect a bias in sampling along the slow axis of symmetry of the strongly anisotropic layer that we resolve here. Alternatively, the low Pn velocities may instead reflect the velocities of the uppermost mantle below the sub-Moho layer, which are assumed to be lower than normal upper mantle (7.8 and 4.3 km/s, respectively for P and S velocities). We also note that receiver functions are insensitive to absolute velocities and we could have used lower overall velocities, which trade off with estimated layer thicknesses, with a similar fit to our data. Finally, this layer appears to be bounded both above and below by sharp interfaces (Figure 5).

We speculate that the sub-Moho, high-velocity layer represents the seismic signature of the thin lithospheric mantle, with a largely Iherzolitic composition [Francis *et al.*, 2010]. The inferred seismic anisotropy may then

be consistent with lattice-preferred orientation of olivine due to internal shearing at the time the lithosphere stabilized or to basal shearing from subsequent tectonic events [e.g., Mazzotti and Hyndman, 2002; Audet et al., 2016]. The very low estimated thickness (~ 10 km) of the Iherzolite layer and shallow lithosphere–asthenosphere boundary (~ 50 km) are consistent with the lower bounds on these values estimated from xenolith data for the Cordillera [Harder and Russell, 2006]. Such a shallow lithosphere–asthenosphere boundary has important implications for the thermal state of the mantle beneath the Cordillera.

Finally, the profile of harmonic components possibly indicates the presence of dipping structures (i.e., interfaces) within the uppermost mantle beneath the Cordillera (Figure 10). These structures may be associated with delamination of a former dense crustal root [e.g., Zandt et al., 2004] or lithospheric mantle [Bao et al., 2014]. These signals coincide with strong radial anisotropy ($V_{SV} > V_{SH}$) observed in this region at 70–150 km depth from the inversion of surface wave data [Yuan et al., 2011], interpreted as downwelling material. This interpretation is consistent with the results of Bao et al. [2014] for the southern Canadian Cordillera and would imply that the high degree of apparent mantle mixing, required for homogeneously high temperatures beneath the Cordillera, may be the result of lithospheric mantle or dense crustal downwelling along the craton edge that produce upwelling of hotter asthenospheric mantle in this region.

7.3. Seismic Anisotropy, Lithosphere Strength, and Geodynamic Models

The crust and uppermost mantle structures imaged by receiver functions, as well as additional seismic data, provide important constraints on the mechanical behavior of the lithosphere during the various tectonic episodes that created the northern Cordillera. As discussed in section 7.1, the Moho geometry points to a removal of the crustal thickness variations that likely resulted from the accretion of the Cordilleran terranes during the Mesozoic. Whether by delamination of the lower crust/uppermost mantle or by extrusion of the middle/lower crust through gravitational collapse, the processes that led to the present-day flat, sharp Moho required an elevated geotherm and mechanical decoupling of the upper crust from the rest of the lithosphere for most of the Cordillera. However, the timing of these events is unknown and the seismic data cannot be used to assert whether this lithospheric strength profile can be extrapolated to the present day.

Seismic anisotropy can also provide strong constraints on the strength profile and mechanical coupling of the lithosphere during the major Cordilleran tectonic events. Combining our anisotropy data from receiver functions with those obtained using core-refracted shear wave (SKS) splitting [Snyder and Bruneton, 2007; Courtier et al., 2010; Rasendra et al., 2014; Audet et al., 2016] provides a detailed picture of variations in crustal and upper mantle anisotropy, both laterally within the Cordillera and vertically throughout the lithosphere (and possibly upper asthenosphere). Figure 12 illustrates the complexity and spatial variability of the anisotropy orientations in the crust (0–30 km), lithospheric mantle (30–60 km), and uppermost mantle (circa 40–100 km). Despite this complexity, and taking into account the limited resolution of the anisotropy orientation, especially in the intermediate 30–60 km depth range, two first-order patterns can be defined:

1. *Consistency of anisotropy orientations with large-scale tectonic structures throughout the lithosphere and uppermost mantle.* This is illustrated by stations in southwestern Yukon near the Denali Fault [cf., Rasendra et al., 2014; Audet et al., 2016] and, to a lesser extent, in central Yukon near the northern section of the Tintina Fault. Mean orientations for stations within ~ 100 km of the Denali Fault trace are N115° (0–30 km), N095° (30–60 km), and N118° (40–100 km), consistent with each other and with the fault orientation (approximately N120–130°) within their variability of about 20–30°. A similar situation is observed for the northern Tintina Fault, except for the 30–60 km depth range where orientations appear much more variable and less robust.
2. *Significant variations in anisotropy orientations at various lithospheric depth ranges.* This situation is best illustrated in southern Yukon, where the anisotropy orientations show clear spatial coherence within a given depth range but strong differences between the three layers. As an example, mean anisotropy orientations along the southern section of the Tintina Fault vary between N150° (0–30 km), N045° (30–60 km), and N105° (40–100 km).

The first case (depth consistency with structures) points to a strong mechanical coupling associated with a major shear fabric developed through the whole lithosphere, likely during the accommodation of approximately 400 km of displacement on the Denali and Tintina Faults in Late Cretaceous-Early Eocene. In contrast, the second case (depth variability) suggests a mechanical decoupling of the crust from the lithospheric

mantle during or posterior to the main Meso-Cenozoic tectonic events. Following Audet *et al.* [2016], the complexity of the anisotropy data in the southern region may reflect the interaction between crustal fabrics, mostly associated with the main tectonic structures, and mantle fabrics affected by the Liard Tectonic Zone, which marks a major boundary between the tectonics and lithosphere structures in the Northern Cordillera and Southern Cordillera.

Although these seismic anisotropy data cannot be used to validate the models proposed for the present-day geodynamic of the northern Cordillera, they provide important constraints that point to the need for some revisions. The consistency of anisotropy orientations throughout the lithosphere with the orientations of the Denali and northern Tintina Faults suggests that processes requiring crust/upper mantle decoupling, such as orogenic float or delamination [e.g., Mazzotti and Hyndman, 2002; Hyndman and Currie, 2011], cannot have erased the inherited vertical shear fabrics. Thus, these processes, if responsible for the present-day tectonics, must have limited cumulative strain, at least near the Denali and northern Tintina Fault regions. Similarly, the uppermost mantle anisotropy directions (SKS and receiver functions) are not compatible with the northeastward mantle flow proposed by Finzel *et al.* [2011, 2014] as a driver for the present regional tectonics. Thus, if present, such an upper mantle flow must produce limited shear within the lithospheric mantle in order not to erase the inherited fabric (in contrast with plate motion marked in SKS on the Canadian craton).

8. Conclusion

Taking advantage of recent seismic experiments, this study provides the first exhaustive analysis of seismic structure and anisotropy in the crust and lithospheric mantle of the Northern Canadian Cordillera. The key elements are (1) flat, sharp (\sim 1–2 km thick) Moho interface over most of the Cordillera; (2) \sim 10 km thick high-velocity sub-Moho layer; and (3) significant anisotropy in the upper crust and uppermost mantle, related to inherited fabric near large-scale Denali and Tintina Faults, but complex in SE Yukon near the Liard transfer zone boundary. Although these results cannot discriminate between the various geodynamic models proposed to explain the present-day tectonics of the Cordillera, they provide strong constraints on these processes, in particular on the fact that neither lower crust/upper mantle decoupling (ogenetic float or delamination) or upper mantle flow can be strong enough to have erased the inherited structural fabric acquired during the Meso-Cenozoic tectonic phases. These results are limited for the most part by the short acquisition period of the new stations. Completion of the Transportable Array deployment in the western part of the study area should improve the lateral resolution of these structures.

Acknowledgments

We thank the various federal, territorial, and municipal agencies in the Yukon and Northwest Territories (Government of Yukon Highway and Public Works, Government of Yukon Energy Mines and Resources, towns of Faro and Norman Wells, British Columbia Wildfire Service, Northwest Territories Environment and Natural Resources, and Nav Canada) for allowing us access to their land in the installation of the Yukon-Northwest Seismograph Network. We also acknowledge constructive comments by D. Schutt and an anonymous reviewer that improved this paper. Data for the NY (doi:10.7914/SN/NY) and TA (doi:10.7914/SN/TA) networks are available from the IRIS Data Management Center at <http://www.iris.edu/hq/>. The IRIS Data Management System is funded through the National Science Foundation (NSF) and specifically the GEO Directorate through the Instrumentation and Facilities Program of the NSF under cooperative agreement EAR-1063471. This work is supported by the Natural Science and Engineering Research Council (Canada) through a Discovery Grant to Audet, by the Ministry of Research and Innovation of Ontario, and by Agence National de la Recherche (France) through grant ANR-12-CHEX-0004-01 to Mazzotti.

References

- Audet, P. (2010), Temporal variations in crustal scattering structure near Parkfield, California, using receiver functions, *Bull. Seismol. Soc. Am.*, **100**, 1356–1362.
- Audet, P. (2015), Layered crustal anisotropy around the San Andreas fault near Parkfield, California, *J. Geophys. Res. Solid Earth*, **120**, 3527–3543, doi:10.1002/2014JB011821.
- Audet, P., M. G. Bostock, D. C. Boyarko, M. R. Brudzinski, and R. M. Allen (2010), Slab morphology in the Cascadia fore arc and its relation to episodic tremor and slip, *J. Geophys. Res.*, **115**, B00A16, doi:10.1029/2008JB006053.
- Audet, P., C. Sole, and A. J. Schaeffer (2016), Control of lithospheric inheritance on neotectonic deformation in northwestern Canada?, *Geology*, **44**, 807–810.
- Audet, P., A. M. Jellinek, and H. Uno (2007), Mechanical controls on the deformation of continents at convergent margins, *Earth Planet. Sci. Lett.*, **264**, 151–166.
- Bao, X., D. W. Eaton, and B. Guest (2014), Plateau uplift in western Canada caused by lithospheric delamination along a craton edge, *Nat. Geosci.*, **7**, 830–833.
- Bianchi, I., J. Park, N. P. Agostinetti, and V. Levin (2010), Mapping seismic anisotropy using harmonic decomposition of receiver functions: An application to northern Apennines, Italy, *J. Geophys. Res.*, **115**, B12317, doi:10.1029/2009JB007,061.
- Bostock, M. G. (1998), Mantle stratigraphy and evolution of the Slave province, *J. Geophys. Res.*, **103**, 21,183–21,200, doi:10.1029/98JB01069.
- Calvert, A. J. (2016), Seismic interpretation of crustal-scale extension in the Intermontane Belt of the northern Canadian Cordillera, *Geology*, **44**, 447–450.
- Cassidy, J. F. (1992), Numerical experiments in broadband receiver function analyses, *Bull. Seismol. Soc. Am.*, **82**, 1453–1474.
- Cecile, M. P., D. W. Morrow, and G. K. Williams (1997), Early Paleozoic (Cambrian to Early Devonian) tectonic framework, Canadian Cordillera, *Bull. Can. Petrol. Geol.*, **45**, 54–74.
- Clowes, R. M., P. T. C. Hammer, G. F. Viejo, and J. K. Welford (2005), Lithospheric structure in northwestern Canada from LITHOPROBE seismic refraction and related studies: A synthesis, *Can. J. Earth Sci.*, **42**, 1277–1293.
- Cossette, E., P. Audet, D. A. Schneider, and B. Grasemann (2016), Structure and anisotropy of the crust in the Cyclades, Greece, using receiver functions constrained by in situ rock textural data, *J. Geophys. Res. Solid Earth*, **121**, 2661–2678, doi:10.1002/2015JB012460.
- Courtier, A. M., J. B. Gaherty, J. Revenaugh, M. G. Bostock, and E. J. Garnero (2010), Seismic anisotropy associated with continental lithosphere accretion beneath the CANOE array, northwestern Canada, *Geology*, **38**, 887–890.

- Currie, C. A., and R. D. Hyndman (2006), The thermal structure of subduction zone back arcs, *J. Geophys. Res.*, **111**, B08404, doi:10.1029/2005JB004024.
- Elliott, J., J. T. Freymueller, and C. F. Larsen (2013), Active tectonics of the St. Elias orogeny, Alaska, observed with GPS measurements, *J. Geophys. Res. Solid Earth*, **118**, 5625–5642, doi:10.1002/jgrb.50341.
- Finzel, E. S., L. M. Flesch, and K. D. Ridgway (2011), Kinematics of a diffuse North America–Pacific–Bering plate boundary in Alaska and western Canada, *Geology*, **39**, 835–838.
- Finzel, E. S., L. M. Flesch, and K. D. Ridgway (2014), Present-day geodynamics of the northern North American Cordillera, *Earth Planet. Sci. Lett.*, **404**, 111–123.
- Finzel, E. S., L. M. Flesch, K. D. Ridgway, W. E. Holt, and A. Ghosh (2015), Surface motions and intraplate continental deformation in Alaska driven by mantle flow, *Geophys. Res. Lett.*, **42**, 4350–4358, doi:10.1002/2015GL063987.
- Flück, P., R. D. Hyndman, and C. Lowe (2003), Effective elastic thickness of the lithosphere in western Canada, *J. Geophys. Res.*, **108(B9)**, 2430, doi:10.1029/2002JB002201.
- Francis, D., W. Minarik, Y. Proenza, and L. Shi (2010), An overview of the Canadian Cordilleran lithospheric mantle, *Can. J. Earth Sci.*, **47**, 353–368.
- Frederiksen, A. W., and M. G. Bostock (2000), Modelling teleseismic waves in dipping anisotropic structures, *Geophys. J. Int.*, **141**, 401–412.
- Frederiksen, A. W., and C. Delaney (2015), Deriving crustal properties from the P code without deconvolution: The southwestern Superior Province, North America, *Geophys. J. Int.*, **201**, 1491–1506.
- Harder, M., and J. K. Russell (2006), Thermal state of the upper mantle beneath the Northern Cordilleran Volcanic Province (NCVP), British Columbia, Canada, *Lithos*, **87**, 1–22.
- Hayward, N. (2015), Geophysical investigation and reconstruction of lithospheric structure and its control on geology, structure, and mineralization in the cordillera of northern Canada and eastern Alaska, *Tectonics*, **34**, 2165–2189, doi:10.1002/2015TC003871.
- Hyndman, R. D., P. Flück, S. Mazzotti, T. J. Lewis, J. Ristau, and L. Leonard (2005), Current tectonics of the northern Canadian Cordillera, *Can. J. Earth Sci.*, **42**, 1117–1136.
- Hyndman, R. D., and C. A. Currie (2011), Why is the North America Cordillera high? Hot backarcs, thermal isostasy, and mountain belts, *Geology*, **39**, 8, 783–786.
- Johnston, S. T. (2008), The cordilleran ribbon continent of North America, *Annu. Rev. Earth Planet. Sci.*, **36**, 495–530.
- Kao, H., Y. Behr, C. A. Currie, R. D. Hyndman, J. Townend, F. C. Lin, M. H. Ritzwoller, S. J. Shan, and J. He (2013), Ambient seismic noise tomography of Canada and adjacent regions: Part 1. Crustal structures, *J. Geophys. Res. Solid Earth*, **118**, 5865–5887, doi:10.1002/2013JB010535.
- Kennett, B. L. N. (1983), *Seismic Wave Propagation in Stratified Media*, 285 pp., Cambridge Univ. Press, U. K.
- Kennett, B. L. N., and E. R. Engdahl (1991), Traveltimes for global earthquake location and phase identification, *Geophys. J. Int.*, **105**, 429–465.
- Leonard, L. J., S. Mazzotti, and R. D. Hyndman (2008), Deformation rates estimates from earthquakes in the northern cordillera of Canada and eastern Alaska, *J. Geophys. Res.*, **113**, B08406, doi:10.1029/2007JB005456.
- Levin, V., and J. Park (1997), P-SH conversions in a flat-layered medium with anisotropy of arbitrary orientation, *Geophys. J. Int.*, **131**, 253–266.
- Levin, V., J. A. vanTongeren, and A. Servali (2016), How sharp is the sharp Archean Moho? Example from eastern Superior Province, *Geophys. Res. Lett.*, **43**, 1928–1933, doi:10.1002/2016GL067729.
- Lewis, T. J., R. D. Hyndman, and P. Flück, P. (2003), Heat flow, heat generation, and crustal temperatures in the northern Canadian Cordillera: Thermal control of tectonics, *J. Geophys. Res.*, **108(B6)**, 2316, doi:10.1029/2002JB002090.
- Licciardi, A., and N. Piana Agostinetti (2016), A semi-automated method for the detection of seismic anisotropy at depth via receiver function analysis, *Geophys. J. Int.*, **205**, 1589–1612.
- Lowe, C., and J. F. Cassidy (1995), Geophysical evidence for crustal thickness variations between the Denali and Tintina fault systems in west-central Yukon, *Tectonics*, **14**, 909–917, doi:10.1029/95TC00087.
- Maréchal, A., S. Mazzotti, J. L. Elliott, J. T. Freymueller, and M. Schmidt (2015), Indentor-corner tectonics in the Yakutat-St. Elias collision constrained by GPS, *J. Geophys. Res. Solid Earth*, **120**, 3897–3908, doi:10.1002/2014JB011842.
- Mazzotti, S., and R. D. Hyndman (2002), Yakutat collision and strain transfer across the northern Canadian Cordillera, *Geology*, **30**, 495–498.
- Mazzotti, S., L. J. Leonard, R. D. Hyndman, and J. F. Cassidy (2008), Tectonics, dynamics, and seismic hazard in the Canada–Alaska Cordillera, in *Active Tectonics and Seismic Potential of Alaska*, vol. 179, edited by J. T. Freymueller et al., pp. 297–319, AGU, Washington, D. C., doi:10.1029/179GM17.
- Monger, J., and R. Price (2002), The Canadian Cordillera: Geology and tectonic evolution, *CSEG Recorder*, **27**, 17–36.
- Mooney, W. D., and M. K. Kaban (2010), The North American upper mantle: Density, composition, and evolution, *J. Geophys. Res.*, **115**, B12424, doi:10.1029/2010JB000866.
- Nelson, J. L., and M. Colpron (2007), Tectonics and metallogeny of the British Columbia, Yukon, and Alaskan Cordillera, 1.8 Ga to the present, in *Mineral Deposits of Canada: A Synthesis of Major Deposit-Types, District Metallogeny, the Evolution of Geological Provinces, and Exploration Methods*, edited by W. D. Goodfellow, *Geol. Assoc. Canada, Mineral Deposits Division. Spec. Publ.*, **5**, 755–791.
- Oldow S. J., A. W. Bally, and H. G. Avé Lallement (1990), Transpression, orogenic float, and lithospheric balance, *Geology*, **18**, 991–994.
- Perry, H. K. C., D. W. Eaton, and A. M. Forte (2002), LITH5.0: A revised crustal model for Canada based on Lithoprobe results, *Geophys. J. Int.*, **150**, 285–294.
- Piana Agostinetti, N., and A. Amato (2009), Moho depth and V_p/V_s ratio in peninsular Italy from teleseismic receiver functions, *J. Geophys. Res.*, **114**, B06303, doi:10.1029/2008JB005899.
- Piana Agostinetti, N., I. Bianchi, A. Amato, and C. Chiarabba (2011), Fluid migration in continental subduction: The northern Apennines case study, *Earth Planet. Sci. Lett.*, **302**, 267–278.
- Porter, R., G. Zandt, and N. McQuarrie (2011), Pervasive lower-crustal seismic anisotropy in Southern California: Evidence for underplated schists and active tectonics, *Lithosphere*, **3**, 201–220.
- Rasendra, N., M. Bonnin, S. Mazzotti, and C. Tiberi (2014), Crustal and upper-mantle anisotropy related to fossilized transpression fabric along the Denali Fault, northern Canadian Cordillera, *Bull. Seismol. Soc. Am.*, **104**, 1964–1975.
- Savage, M. K. (1998), Lower crustal anisotropy or dipping boundaries? Effects on receiver functions and a case study in New Zealand, *J. Geophys. Res.*, **103**, 15,069–15,087, doi:10.1029/98JB00795.
- Schimmel, M., and H. Paulssen (1997), Noise reduction and detection of weak, coherent signals through phase-weighted stacks, *Geophys. J. Int.*, **130**, 497–505.
- Shioiri, K., and J. Park (2008), Structural features of the subducting slab beneath the Kii Peninsula, central Japan: Seismic evidence of slab segmentation, dehydration and anisotropy, *J. Geophys. Res.*, **113**, B10318, doi:10.1029/2007JB005,535.

- Snyder, D., and M. Bruneton (2007), Seismic anisotropy of the Slave craton, NW Canada, from joint interpretation of SKS and Rayleigh waves, *Geophys. J. Int.*, 169, 170–188.
- Thomson, C. J. (1996), Notes on waves in layered media to accompany program Rmatrix, in *Seismic Waves in Complex 3-D Structures*, pp. 147–162, Department of Geophysics, Charles Univ., Prague.
- Wetmiller, R. J., R. B. Horner, H. S. Hasegawa, R. G. North, M. Lamontagne, D. H. Weichert, and S. G. Evans (1988), An analysis of the 1985 Nahanni earthquakes, *Bull. Seismol. Soc. Am.*, 78, 590–616.
- Xu, L., S. Rondenay, and R. D. van der Hilst (2007), Structure of the crust beneath the southeastern Tibetan Plateau from teleseismic receiver functions, *Phys. Earth Planet. Int.*, 165, 176–193.
- Yuan, H., B. Romanowicz, K. M. Fischer, and D. Abt (2011), 3-D shear-wave radially and azimuthally anisotropic velocity model of the North American upper mantle, *Geophys. J. Int.*, 184, 1237–1260.
- Zandt, G., and C. J. Ammon (1995), Continental crust composition constrained by measurements of crustal Poisson's ratio, *Nature*, 374, 152–154.
- Zandt, G., H. Gilbert, T. J. Owens, M. Ducea, J. Saleeby, and C. H. Jones (2004), Active foundering of a continental arc root beneath the southern Sierra Nevada in California, *Nature*, 431, 41–46.
- Zhu, L., and H. Kanamori (2000), Moho depth variation in southern California from teleseismic receiver functions, *J. Geophys. Res.*, 105, 2969–2980, doi:10.1029/1999JB900322.